ORIGINAL RESEARCH ARTICLE

Cold Metal Transfer Welding of Ferritic and Austenitic Stainless Steel: Microstructural, Mechanical, and Electrochemical Studies

Santosh K. Gupta, Awanikumar P. Patil, Ramesh C. Rathod, Aman Gupta, Hitesh Methani, and Vipin Tandon

In the present study, cold metal transfer arc welding was employed to weld the 304L austenitic stainless steel (ASS) and Ti-stabilized 439 ferritic stainless steel (FSS) using a 309L filler electrode. Dissimilar joints were prepared using low heat input (HI; W1 ∼ 247 J/mm) and high HI (W2 ∼ 282 J/mm). The solidification mode for both weldments were the ferritic-austenitic mode and the weld zone (WZ) regions of both the weldments consists of columnar austenites, lathy and skeletal ferrite phases. The interfaces between WZ and ASS base metal showed the unmixed zone, whereas a conventional heat-affected zone (HAZ) was formed between the WZ and FSS base metals. The formation of ferrite stringers were observed in the unmixed zone, whereas peppery features of chromium-rich carbides were observed in HAZ. Moreover, electron backscattered diffraction technique was used to distinguish the microstructural differences between W1 and W2 weldments. Increase in the HIs resulted in decreased ferrite fraction in WZ as well as decrease in the mechanical strength of the joints. The W1 weldment depicted higher values of average micro-hardness (WZ ≈ 334.32 HV) than W2 (WZ ≈ 310.92 HV)) weldment. The electrochemical behaviour of the weldments was analysed for both the base metals and WZ of weldments. The higher degree of sensitization (DOS ∼ 9.24%) of W1-WZ showed lower intergranular corrosion resistance than W2-WZ (DOS ∼ 7.77%), however, the opposite trend was observed for impedance and pitting resistance.

Abbreviations	
ASS	Austenitic stainless steel
BM	Base metal
CGHAZ	Coarse grain heat affected zone
CMT	Cold metal transfer
Cr_{eq}	Chromium equivalent
%D	% Dilution
DLEPR	Double-loop electrochemical potentiodynamic reactivation
DMW	Dissimilar metal welding
DOS	Degree of sensitization
EBSD	Electron back-scattered diffraction
EDS	Energy-dispersive spectroscopy
EIS	Electrochemical impedance spectroscopy
FGHAZ	Fine grain heat affected zone
FSS	Ferritic stainless steel
GBs	Grain boundaries
HAZ	Heat affected zone
HI	Heat input
IGC	Intergranular corrosion
LF	Lathy ferrite
Ni_{eq}	Nickel equivalent
OM	Optical microstructure
PDP	Potentiodynamic polarization
SEM	Scanning electron microscope
SF	Skeletal ferrite
SSs	Stainless steel
UMZ	Unmixed zone
WZ	Weld zone
XRD	X-ray diffraction

1. Introduction

In various industrial scenarios, there are instances where it becomes necessary to join dissimilar materials. And, the selection of these materials depends on their specific location within a structure, aiming to effectively and economically utilize the unique properties offered by each material. Also, nowadays, industries now use a variety of materials to fabricate their products to increase durability, performance, and economic production (Ref 1). Austenitic stainless steels (ASSs) are an attractive material to various industries ascribed to their

Santosh K. Gupta, Awanikumar P. Patil, and Ramesh C. Rathod, Department of Metallurgical and Materials Engineering, Visvesvaraya National Institute of Technology, Nagpur 440010, India; Aman Gupta, Department of Advanced Components and Materials Engineering, Sunchon National University, Suncheon 57922, Republic of Korea; and Division of Research and Development, Lovely Professional University, Phagwara 144411, India; Hitesh Methani, Department of Mechanical Engineering, Thapar Institute of Engineering and Technology, Patiala 147004, India; and Vipin Tandon, Centre of Sustainable Built Environment, Manipal School of Architecture and Planning, Manipal Academy of Higher Education, Manipal 576104, India. Contact e-mails: amangpta@gmail.com, vipintandon3103@gmail.com and vipin.tandon@manipal.edu.

excellent mechanical and electrochemical characteristics (Ref 2). But, the presence of higher fraction of Ni enhances the cost of the ASS products. On the other side, ferritic stainless steels (FSSs) having low Ni content, demonstrate the possibility of a cost-effective option to replace the ASS grades in various applications (Ref 3). In addition to the cost advantages, FSSs exhibit better resistance to stress corrosion cracking than ASSs when exposed to caustic and alkaline conditions (Ref 4). The joining of dissimilar materials can produce the desired characteristics and showed greater adaptability in service conditions (Ref 5). Moreover, among the various bimetallic combinations, the ASS-FSS joints are widely employed in industrial domains such as nuclear power generation, pressure vessels, heat exchangers, and paper industries, etc. (Ref 6, 7). Usually, the combination of ASS-FSS is employed in $TiCl_4$ reduction retorts (Ref 7).

Dissimilar metal welding (DMW) of ASS-FSS is usually performed using conventional welding techniques like shielded metal arc welding (SMAW), gas tungsten arc welding (GTAW), and gas metal arc welding (GMAW), etc. However, attributed to the variance in materials metallurgical, physical, and mechanical properties, and as well as the frequent use of high heat input (HI) during fusion welding processes, DMW is a challenging task to produce the sound joints by using conventional welding processes (Ref 8). During the ASS-FSS DMW, solidification cracking, hot cracking, weld decay, and knife-line attack occur on the ASS side of the weldment. Whereas the weldments of the FSS side experience the coarsening of grains in heat-affected zone (HAZ) and weld zone (WZ), which reduces the weldment ductility and toughness (Ref 9). Furthermore, the welding process introduces a weld thermal cycle that can lead to the formation of carbide precipitates and various phases, giving rise to additional concerns such as sensitization, which greatly influences the corrosion resistance properties of the weldments (Ref 10). Numerous investigations have been conducted on different fusion and solid-state welding techniques for DMW involving ASS and FSS (Ref 7, 11-13). Emami et al. (Ref 7) investigated the DMW of 304L ASS and 430 FSS utilizing friction-stir welding. Their findings revealed the existence of both austenite and ferrite phases in the stir zone. The authors further noted that the fracture in the tensile test occurred in the FSS base metal (BM), attributing it to lower ductility compared to the ASS BM (Ref 7). In our earlier work (Ref 11), we have studied the influence of process parameters in dissimilar welding of 304L and 439 FSS via GTAW process. It was concluded that dual-phase (δ-ferrite and austenite) microstructure formed in WZ of low and high HI weldments. The mechanical characteristics exhibited better properties for low HI weldment (Ref 11).

CMT welding technique is the modified version of the conventional GMAW technique which offers the advantages of both low HI without any welding flaws (Ref 14). The CMT arc welding process differs from conventional welding techniques by the liquid droplet mode, which is detached by the electrode wire at a faster rate, uses controlled HI, and produces less spatter when the filler wire short-circuits to the workpiece (Ref 15). Koli et al. (Ref 16) reported that on employing similar welding currents for CMT, metal inert gas (MIG) and pulsed MIG processes on Al alloys, the CMT process demonstrated better bead penetration than its counterparts. Frostevarg et al. (Ref 17) studied the comparison of three distinct arc modes (standard, CMT, and pulsed mode) in laser-arc hybrid welding of Domex 420 MC D steel (7 mm, EN-10149-2) and concluded

that the CMT arc mode resulted in the formation of a narrower HAZ as compared to the other modes. However, no discussions about the microstructure evolution were discussed for three-welding processes (Ref 17). According to Dharmik et al. (Ref 18), CMT-welded (similar welding) 0.5 mm electrical sheets depicted smaller HAZ due to less HI and smaller grain size (GS) than MIG and GTAW welding. Further, numerous investigations have been conducted on different conventional and CMT welding processes for similar welding of FSS. Zhou et al. (Ref 19) studied the welding characteristics (microstructural and mechanical) of similar welding of 430 FSS using the CMT technique by employing a 308L filler electrode. The authors have reported that the WZ consisted of dual-phase (ferrite and austenite) microstructure and HAZ consisted of chromium-rich carbide ($M_{23}C_6$, where M mainly stood for Cr and Fe) precipitates in ferrite grains and intergranular martensite at ferrite grain boundaries (GBs) (Ref 19). Also, the dual-phase microstructure of WZ causes to increase in the tensile properties and micro-hardness of welded specimens than the BM (Ref 19). In our earlier work (Ref 20), we have studied the influence of process parameters in similar welded 439 FSS (Ti-stabilized) via the CMT welding technique with varying HIs. It was concluded that dual-phase (δ-ferrite and austenite) microstructure formed in WZ of low and high HI weldments. The mechanical characteristics (microhardness and tensile properties) exhibited better properties for low HI weldment, and for IGC resistance, opposite trend was observed as compared to the high HI weldment.

The previous literature makes clear that a lot of research is reported on similar welding of several of steel via conventional and CMT processes (Ref 17-20). However, the mentioned kinds of literature on CMT welding mainly focused on the microstructural and mechanical characteristics of welded specimens of SSs but did not address the electrochemical behaviour of welded specimens of SSs. Also, based on the literature discussed (Ref 7, 11-13), the DMW of the ASS-FSS has not been the subject of any research, i.e. 304L ASS with 439 FSS by employing the CMT welding technique. The 439 FSS used in this study is stabilized by Ti and has a lower content of C, which reduces the possibility of carbide precipitate formation during welding (Ref 20). Hence, the objective of the present study is to study the impact of the CMT welding parameter (HI) on the welding properties (microstructural, mechanical, and electrochemical) of DMW of 304L ASS-439 FSS by employing 309L as a filler electrode.

2. Experimental

2.1 Materials and Method

The BMs (439 FSS and 304L ASS; 3 mm thickness) were subjected to a solution annealing process. The 304L BM was treated at a temperature of 1050 °C, while the 439 BM was treated at 850 °C. Both treatments lasted for 1 h and followed by quenching in water. The major elements present in the chemical composition of BMs, i.e. 304L includes (C- 0.037%, Cr- 18.9%, Ni- 9.32%, Mn- 1.65%, Fe- balance) and 439 includes (C- 0.024%, Cr- 17.35%, Ni- 0.18%, Mn- 0.29%, Ti- 0.25% Fe- balance). The chemical composition of 309L filler electrode includes (C- 0.03%, Cr- 23.65%, Ni- 13.3%, Mn- 0.8%, Fe- balance). Dimensions of 60 mm × 150 mm were cut

Table 1 Welding parameters used in the present study

Sample	Current, A	Voltage, V	Welding speed, mm/s	Heat input, J/mm
W1 (Low HI)	150	12.8	6.6	247.27
W2 (High HI)	130	12.5	4.9	281.88

from annealed BMs sheets using the wire-cut electro-discharge machine for further joining process. Using the CMT technique and 309L as a filler electrode, DMW of 304L ASS-439 FSS was carried out. Table 1 depicts the parameters that are used during the DMW process, and the HI was calculated accordingly by Eq 1 (Ref 20).

$$HI = \eta VI/v \tag{Eq 1}$$

where, "I" and "v" represent welding current (amperes, A) and welding speed (mm/s), respectively, "V" represents arc voltage (volts, V) and "η" represents the welding efficiency, which was 85% for the CMT welding process (Ref 20). It can be observed from Table 1 that changes in the welding current and welding speed were adopted for varying the HIs between two weldments. According to the calculated HIs, the weldments were assigned the designations as W1—lower HI weldment and W2—higher HI weldment.

2.2 Microstructural Characterization

Figure 1 shows a schematic presentation of a weldment in addition to illustrations of various specimens used to examine microstructural features, mechanical properties, and corrosion characteristics. Both the samples were subjected to polishing using emery papers with varying grit sizes (ranging till 2000). This was followed by polishing with a cloth smeared with an alumina slurry (0.75 μm). To reveal the microstructural characteristics, weldments were then subjected to electrochemical etching using a Potentiostat (Solartron, 1285). For the electrochemical etching procedure, a voltage of 6 V was applied for a duration of 30 s, which was carried out in a solution consisting of 100 ml of distilled water containing cupric acid (15 g). To examine the optical microstructure (OM) of the various weldment zones (BM, HAZ, and WZ), the Leica DMi8 optical microscope was used. To identify the various phases that developed in WZ, and in the HAZ region of both weldments, x-ray diffraction (XRD) X'Pert PRO PAN analytical was used. The detailed microstructural evolution and chemical composition of different phases were examined using a scanning electron microscope (SEM—JEOL 6380A, Japan) equipped with an energy-dispersive spectrometer (EDS). The detailed microstructural characteristics of the W1 and W2 weldments were observed using electron back-scattered diffraction (EBSD). Further, the micro-texture analysis was conducted using a Bruker E-flashed HD EBSD detector within the SEM system (Carl Zeiss Sigma 500). The samples were electropolished at 16 V for 16 s in an 80 (ethanol): 20 (perchloric) solution to prepare it for the EBSD. A large area of the weldment was considered for the scanning purpose. Area of 2500 $\times$ 500 μm^2 and step sizes of 1.5 μm were considered for the ESBD measurement of both the weldments. Further to that, high resolution microstructure was also observed by increasing the resolution of the measurement. For that

purpose, scan area of 250 $\times$ 250 μm^2 and step sizes 0.7 μm were used for measuring the WZ region of both the weldments. EBSD measurements were performed at 20 kV voltage and 15 mm working distance, and the data obtained was processed in TSL-OIM software (Ref 21). Inverse pole figure (IPF), phase map, grains size and image quality (IQ) maps were obtained from the EBSD data. A mild clean-up of 0.03 neighbour CI correlation and confidence index > 10% was used to process the EBSD data.

2.3 Mechanical Characterization

The micro-hardness and tensile testing were conducted for both the weldments to assess its mechanical properties. The micro-hardness of the weldments were measured using a Shimadzu micro-hardness testing machine; the load of 300 g stress was applied for a duration 10 s. Figure 1(c) shows the tensile sample dimension, and the experiments were conducted in Instron 4467 universal testing machine, in accordance with the ASTM E8 M-04 standard (Ref 22). Additionally, SEM was utilized to investigate the fracture surfaces.

### 2.4 Electrochemical Characterization

Electrochemical tests were studied on the BMs and WZs of both weldments using a potentiostat (Biologic VMP-300). These tests included the double-loop electrochemical potentiodynamic reactivation test (DLEPR), electrochemical impedance spectroscopy (EIS), and potentiodynamic polarization (PDP). The electrochemical experiments were conducted using a traditional three-electrode cell setup, wherein platinum was implemented as the counter electrode, the sample acted as the working electrode, and a saturated calomel electrode (SCE) was utilized as the reference electrode.

To assess IGC, the DLEPR test was performed in room temperature in a solution containing 0.5 M H_2SO_4 and 0.01 M NH_4SCN. The DLEPR test involved scanning the potential from -500 mV$_{SCE}$ to $+ 300$ mV$_{SCE}$ in the forward direction and from $+ 300$ mV$_{SCE}$ to -500 mV$_{SCE}$ in the reverse direction at a 1.67 mV/s scan rate in room temperature. Further, the EIS and PDP tests were performed in room temperature in a 3.5% NaCl solution in room temperature. In EIS, a 10 mV sinusoidal AC pulse was applied over a frequency range of 10^6 to 10^{-2} Hz. The PDP test involved scanning the potential from -500 mV$_{OCP}$ to $+ 1200$ mV$_{OCP}$ at 0.5 mV/s scan rate. The data obtained from the electrochemical tests were analyzed using the EC-Lab software. All the tests (mechanical and electrochemical) were repeated three times to ensure the reproducibility of data, and the average results are reported in the present study.

3. Results and Discussion

3.1 Microstructural Evolution

The OMs and XRD spectra of the BMs, i.e. 304L ASS and 439 FSS are shown in Fig. 2. The 304L BM showed the coarse austenitic grains with the presence of annealing twins (Fig. 2a) and its XRD spectrum (Fig. 2b) confirmed the existence of the austenite phase only. Similarly, grains in 439 BM were homogenized and equiaxed (Fig. 2c). The 439 BM XRD spectrum (Fig. 2d) confirmed the existence of a single ferritic phase. The macrostructure of the cross section for both the weldments is depicted in Fig. 3(a) and (b) and the sound joint can be observed.
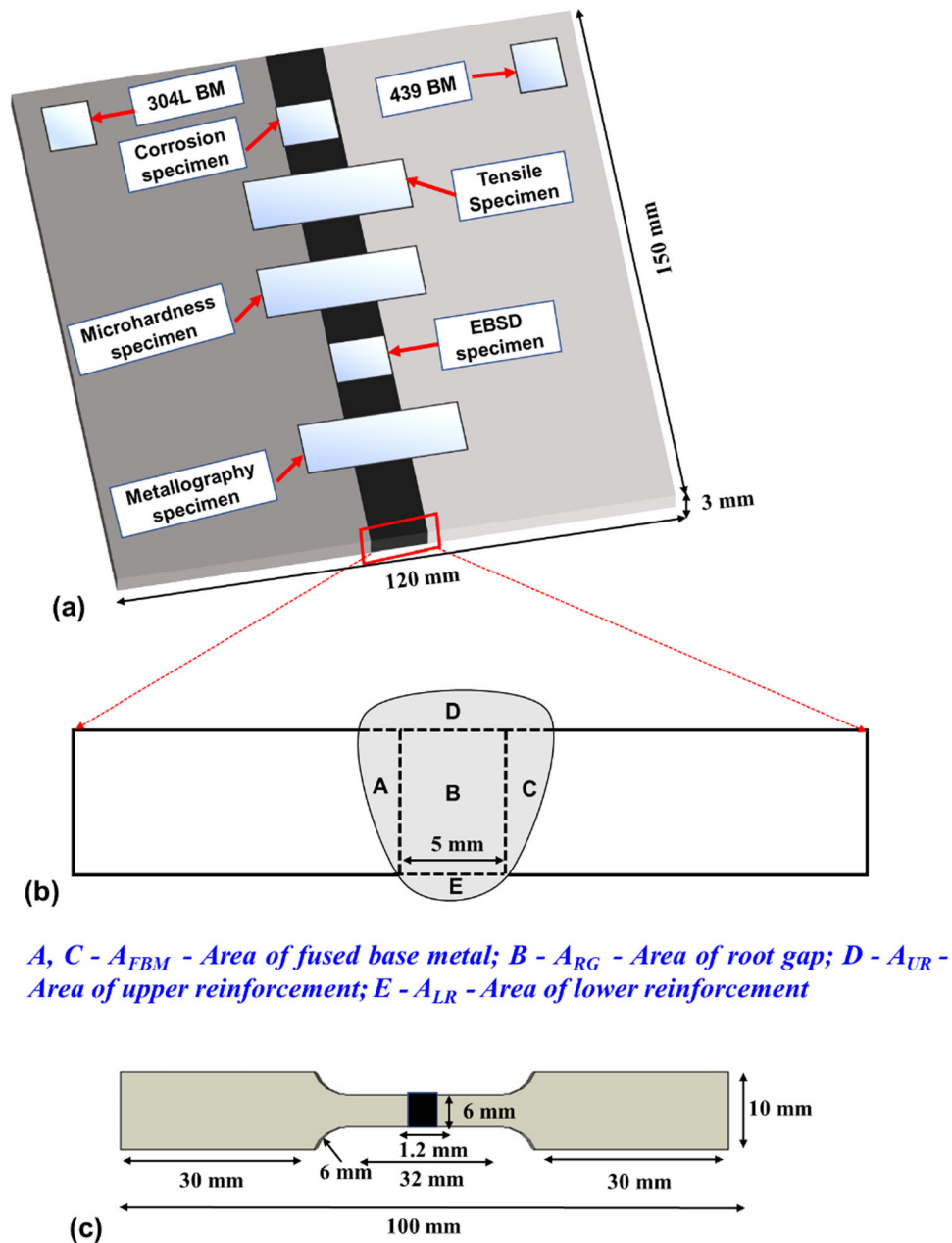
Fig. 1 (a) Schematic diagram of dissimilar welded joint; representative locations of the different specimens considered for the microstructural, mechanical, and corrosion characterization; (b) schematic diagram of weld bead profile; (c) dimensions of the tensile samples used in the present investigation (Color figure online)

The welds displayed complete penetration throughout their entire depth, with no visible macroscopic defects such as cracks, porosity, or undercuts. To determine the percentage dilution (% D), the geometrical areas were measured of both the weldments, as illustrated in Fig. 1(b) and the data are summarized in Table 2. The overall fusion of the BMs $(A_{FBM})_{TOTAL}$ was computed using Eq 2, while the total amount of weld deposition $(A_{WD})_{TOTAL}$ was calculated using Eq 3. Consequently, Eq 4 was employed to determine the % D for both weldments (Ref 23).

$$(A_{FBM})_{TOTAL} = (A_{FBM})_{ASS} + (A_{FBM})_{FSS} \qquad \text{(Eq 2)}$$

$$(A_{WD})_{TOTAL} = A_{UR} + A_{RG} + A_{LR} + (A_{FBM})_{TOTAL} \qquad \text{(Eq 3)}$$

$$\%D = \frac{A_{(FBM)TOTAL}}{A_{(WD)TOTAL}} \qquad \text{(Eq 4)}$$

Notably, Table 2 shows that the % D is influenced by the welding parameters (welding speed and current). During welding, the degree of mixing of BMs and filler electrodes has a substantial influence on the amount of ferrite and the mode of solidification; the solidification mode can vary from ferritic (F) to ferritic-austenitic (FA) and fully austenitic (A) (Ref 24). Consequently, it is crucial to ascertain the %D of the weldments and its solidification mode. For the current investigation, the calculated %D is shown in Table 2 and is for 23.75% for W1 and 18.24% for W2. The higher welding current and speed in W1 were attributed to higher dilution.
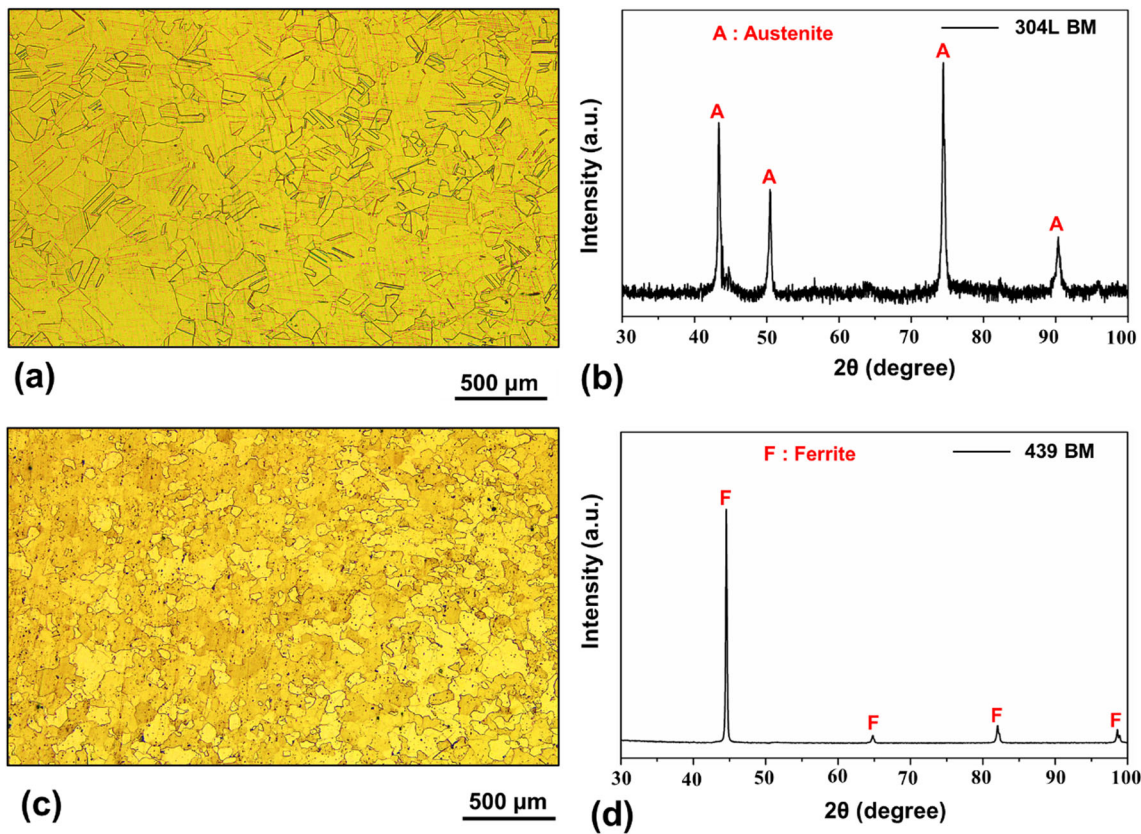
Fig. 2 (a) Optical micrograph (OM) and (b) XRD pattern of 304L BM; (c) OM and (d) XRD pattern of 439 BM (Color figure online)

According to the report, higher welding currents lead to increased arc force and enhanced arc penetration, resulting in greater melting of the BM and subsequently leading to higher dilution (Ref 25).

To estimate the solidification mode, in the current investigation, the stabilizing elements weight (%) of ferrite and austenite was used to determine the chromium equivalent (Cr_{eq}) as well as nickel equivalent (Ni_{eq}) which is mentioned in Table 2. The Cr_{eq}/Ni_{eq} ratio was determined to be 1.66 for the weldment of W1 and 1.59 for the weldment of W2. The difference in the % D between the two weldments primarily contributed to the variation in the Cr_{eq}/Ni_{eq} ratio (Table 2). As per Eq. 5 (Ref 20), both weldment's solidification mode was the FA mode. FA mode can be mentioned as follows:

$$FA : L \rightarrow (L + \delta) \rightarrow (L + \delta + \gamma)$$
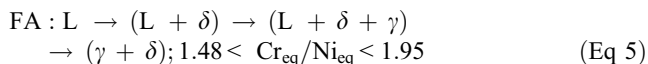$$\rightarrow (\gamma + \delta); 1.48 < Cr_{eq}/Ni_{eq} < 1.95 \qquad (Eq\ 5)$$

Figure 3(c) and (d) depicts the OMs of the W1-WZ and W2-WZ, respectively. It is evident from Fig. 3(c) and (d) that both weldments exhibit a dual-phase microstructure, characterized by the presence of austenite (light-coloured grains) and ferrite phases (dark features), which is in good agreement with the solidification mode, i.e. FA (Eq 5). Also, the different forms of ferrite formation can be seen in both the weldments (Fig. 3c and d). The formation of lathy ferrite (LF) within the austenite matrix was observed in W1-WZ (Fig. 3c), whereas, the formation of skeletal ferrite (SF) within austenite matrix was observed in W2-WZ (Fig. 3d). It is reported when the cooling rate is moderate and solidification takes place in the FA range, the initial solidification occurs with the formation of ferrite,

followed by the subsequent formation of austenite along the boundaries of the ferrite cells and dendrites (Ref 26). The formation of the SF is a result of the progressive advancement of austenite, which gradually consumes the adjacent ferrite through a diffusion-controlled reaction. This process continues until the ferrite becomes sufficiently enriched in elements that favour ferrite formation (such as Cr and Mo) and depleted in elements that promote austenite formation (such as Ni and N) (Ref 12, 26). And, the high cooling rate has probably restricted the diffusion of stabilizing elements during F $\rightarrow$ A transformation, consequently LF forms instead of SF (Ref 27). In the present investigation, the higher cooling rates in the W1-WZ caused the formation of an LF microstructure. In contrast, the W2-WZ exhibited a slower cooling rate than the W1 weldment, resulting in the formation of SF. Figure 3(e) depicts the XRD spectrum of W1-WZ and W2-WZ, revealing the presence of peaks corresponding to both ferrite and austenite phases. No intermetallic precipitates were seen in the spectrum. Therefore, the XRD findings provide additional confirmation of the existence of a dual-phase (ferrite and austenite) microstructure in the W1-WZ and W2-WZ of the weldments. However, due to differences in the thermal cycle and cooling rate, variations in the volume of ferrite fraction occurred. The estimation of ferrite fraction was calculated using the formula mentioned in (Ref 28). The fraction of the ferrite phase was calculated to be 36.86% for the W1-WZ and 33.02% for the W2-WZ. Due to the faster cooling rate in the W1 weldment, the ferrite fraction is higher compared to the W2 weldment. This rapid cooling restricts the F $\rightarrow$ A transformation during the FA solidification mode from taking place.
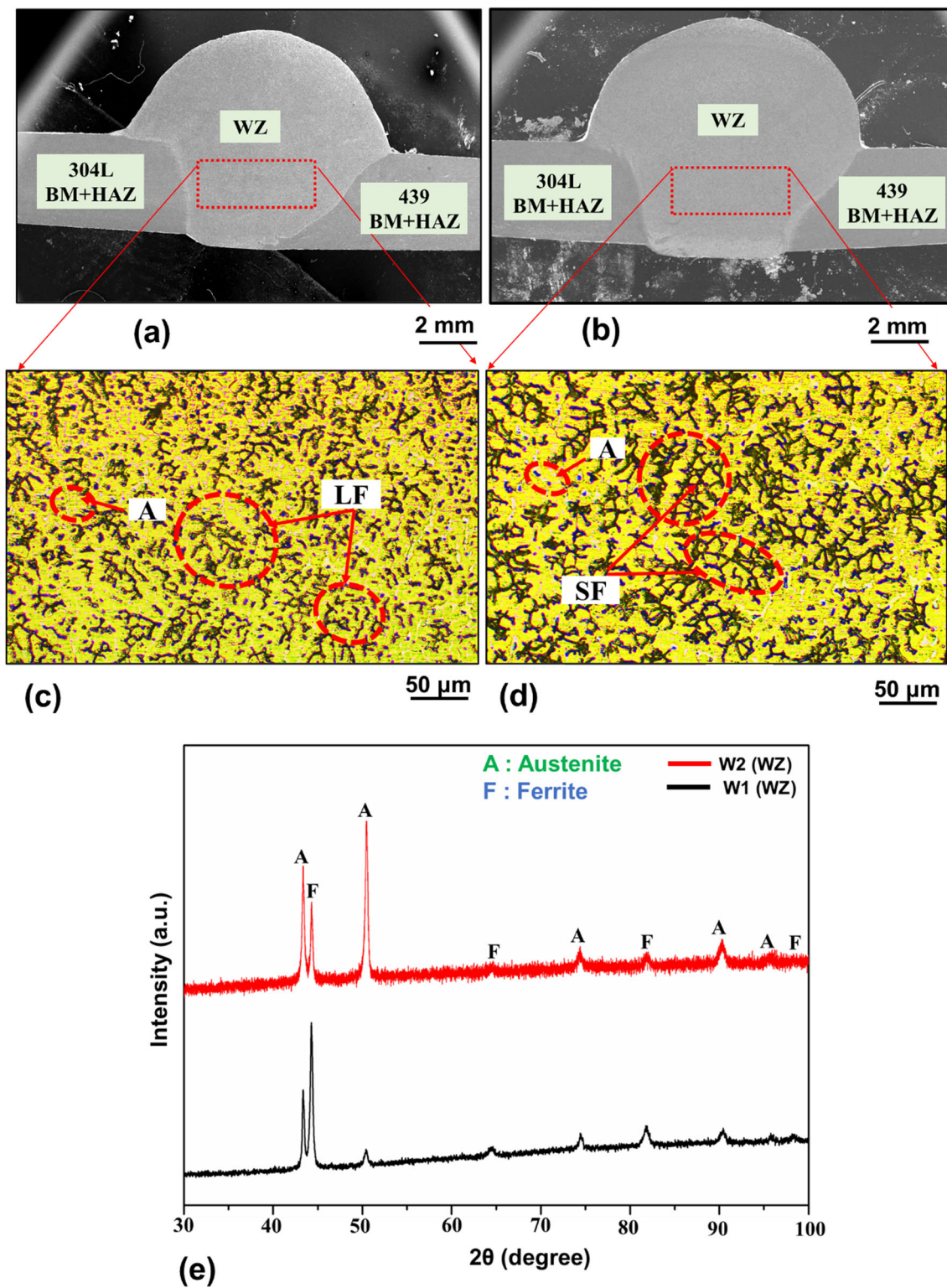
Fig. 3 Macrostructure of (a) W1 and (b) W2 weldment; OMs of WZ and magnified WZ of (c) W1 and (d) W2 weldments; (e) XRD spectrum of WZ of W1 and W2 weldments. **Note:** W1-low HI and W2-high HI, LF-lathy ferrite, SF-skeletal ferrite, A-austenite (Color figure online)

The SEM-EDS analysis of the WZ in both weldments is presented in Fig. 4. The elemental distribution at different locations allows the examination of alloying element distribution in both phases. In Fig. 4, it can be observed that region 1 exhibits a higher composition of Ni and Mn (austenite stabilizing elements), providing confirmation of the presence of the austenite phase. Conversely, region 2 displays a higher composition of Cr (ferrite stabilizing elements), further confirming the presence of the ferrite phase in that specific region.

Detailed microstructural features evolved in the weldments is presented in Fig. 5. Figure 5(a) and (b) illustrates the WZ, unmixed zone (UMZ) next to the WZ, HAZ, and BM of 304L

Table 2 Weld metal dilution calculation with Cr_{eq}/Ni_{eq} ratio

Sample	$A_{304L\ (FBM)}$, mm^2	$A_{439\ (FBM)}$, mm^2	% D, 304L BM	% D, 439 BM	A_{BMF}/mm^2, Total	A_{TWD}/mm^2, Total	% D	Cr_{eq}	Ni_{eq}	Cr_{eq}/Ni_{eq}
W1	4.95	8.37	20.84	14.92	13.32	56.08	23.75	21.81	13.09	1.66
W2	5.02	6.31	8.08	10.16	11.33	62.08	18.24	22.66	14.22	1.59
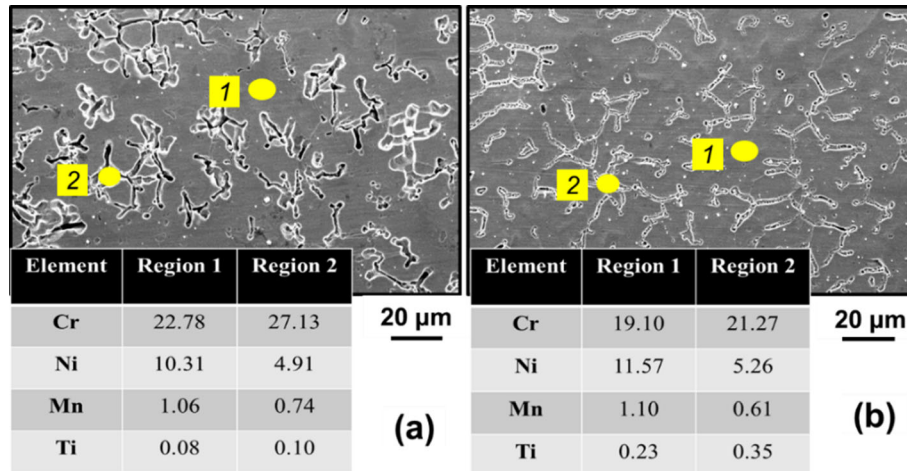
Fig. 4 SEM-EDS analysis of WZ of (a) W1 and (c) W2 weldments. *Note*: Region 1 represents the chemical compositions of austenite matrix, and region 2 represents the chemical compositions of different types of ferrite (Color figure online)
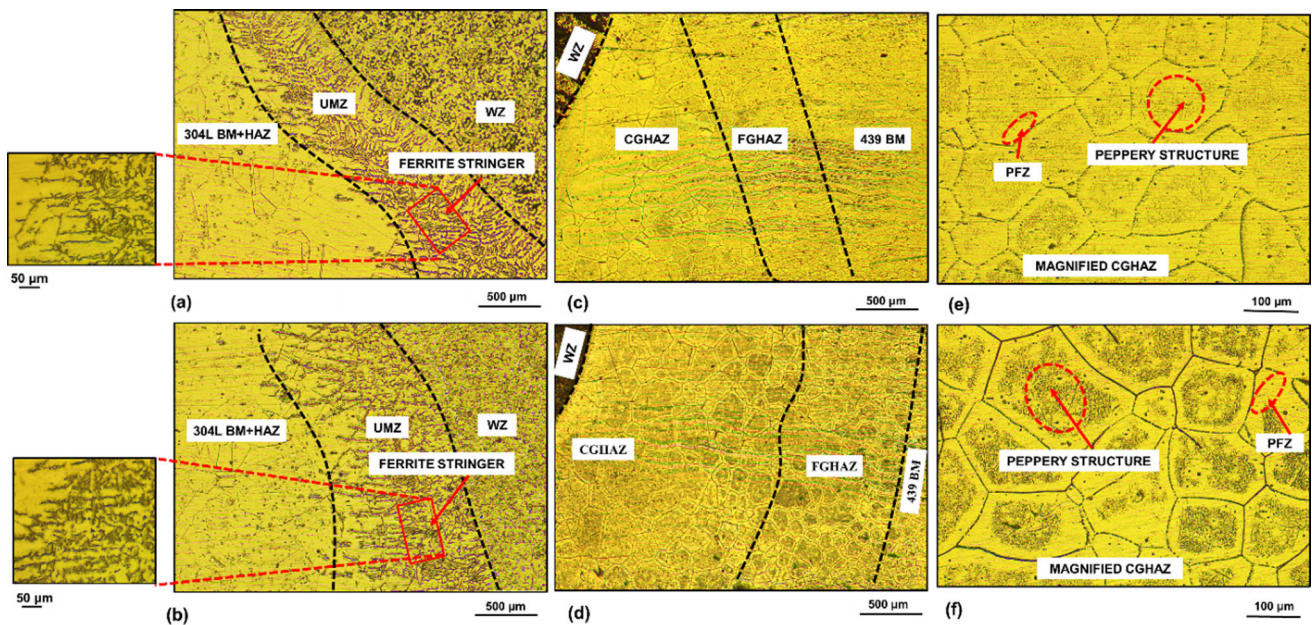

Fig. 5 (a) UMZ of ASS side of W1 weldment, (b) UMZ of ASS side of W2 weldment, (c, e) HAZ and magnified CGHAZ of FSS side of W1 weldment, and (d, f) HAZ and magnified CGHAZ of FSS side of W2 weldment (Color figure online)

ASS. The UMZ has formed next to the FB due to variation in melting point, when the filler materials have a melting point that is comparable to or higher than that of the BM, only a small fraction of the BM melts, and there is no dilution occurs during the solidification (Ref 29). In Fig. 5(a) and (b), the presence of δ-ferrite stringers can be observed in the UMZ near the fusion boundary of the ASS side. This occurrence can be attributed to the dominance of a faster cooling rate and heat flow direction in this area attributed to the ASS lower thermal conductivity than FSS (Ref 13, 30). Figure 5(c), (d), (e) and (f) demonstrates the low magnification OMs of the HAZ region of the FSS side of both weldments. Notably, the HAZ can be divided into two regions in both weldments: coarse grain HAZ (CGHAZ) and fine grain HAZ (FGHAZ), as depicted in Fig. 5(c) and (d). The
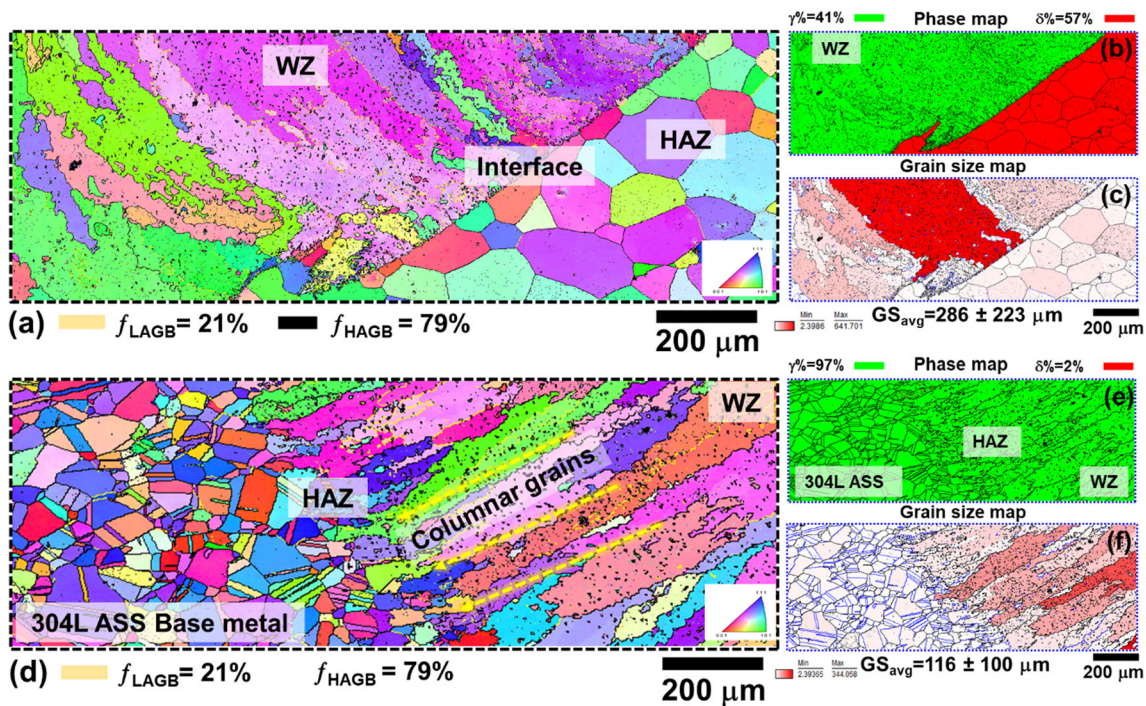
Fig. 6 (a-c) Inverse pole figure (IPF) map, phase map and grain size map of W1 weldment consisting the region of HAZ, WZ and interface between the HAZ and WZ. (d-f) IPF map, phase map and grain size map of W1 weldment consisting the region of WZ, 304L ASS BM and interface between the WZ and 304L ASS BM. *Note:* In phase map—red and green colour represent ferrite and austenite phase, respectively. Twin boundaries are the combined $\Sigma 3 + \Sigma 9$ boundaries (blue colour) (Color figure online)

distinction between these regions is based on the variation in GS, which is influenced by the temperature gradient experienced during and after the welding process (Ref 22). The measured average grain size (GS_{avg}) for CGHAZ was ~ 252 μm for W1 and ~ 300 μm for W2 weldments, whereas for FGHAZ, the GS_{avg} was ~ 112 μm for W1 and ~ 130 μm for W2 weldments. CGHAZ was observed as a result of the grain coarsening caused by the elevated temperature and reduced cooling rate near the fusion boundary. While as move away from the fusion boundary in the HAZ, a drop in temperature and a faster cooling rate occur. These conditions lead to the formation of fine grains, resulting in FGHAZ being observed (Ref 22, 31). Further, Fig. 5(e) and (f) depicts the presence of precipitates that have formed within the ferrite grains in the HAZ regions, which are commonly referred to as the "peppery structure." (Ref 26, 28). Precipitation during cooling is motivated primarily by the lesser solubility of C in the ferrite phase at lower temperatures (Ref 26). Since precipitates were formed at a distance from GBs and hence the area nearby to GBs where there are no precipitates is called as the "precipitate-free zone (PFZ)."

In order to know detailed information about the microstructure and its phase fraction, EBSD characterization was performed for the W1 and W2 weldments. The inverse pole figure (IPF), phase and grain size maps for the W1 weldment consisting of HAZ (near 439 FSS BM), the interface between HAZ and WZ regions is shown in Fig. 6(a), (b) and (c). The respective regions are marked in Fig. 6(a) where clear differences can be observed in the evolved microstructure during the welding. Equiaxed coarse ferrite grains (HAZ) along with the elongated coarse columnar grains (WZ) were observed in the IPF map. Interestingly, the interface between the two regions seems to have well-defined GBs. As discussed in

Fig. 5(c) and (d) that there was a formation of CGHAZ and FGHAZ near the 439 FSS side. CGHAZ seems to have a higher width as compared to FGHAZ and hence in Fig. 6(a), the indicated HAZ refers to the CGHAZ. Phase fraction toward the FSS sides indicates the $\sim 57\%$ of ferrite and $\sim 41\%$ of austenite phase. In the WZ, most of the grains were attributed to the austenite morphology; However, LF and SF are available in very low fractions (Fig. 6b). GS_{avg} was calculated for the 439 FSS side region of the W1 weldment which infers the value of $\sim 286 \pm 223$ μm. EBSD measurement was performed from one end of the weldment (439 FSS side) to another end of the W1 weldment (304L ASS side).

Figure 6(d), (e) and (f) shows the IPF, phase, and GS maps for the austenitic side regions of the W1 weldment. IPF clearly distinguishes the GBs for the austenite phase as it was not observed in the OMs (shown in Fig. 3). Orientations of every grain attributed to different colours to the grains present in the WZ as well as other regions of the austenitic side. In the WZ, there was coarse columnar austenitic grains were formed after the welding as it was marked with the yellow colour arrows (Fig. 6d). Substantial differences can be observed in the WZ of 304L ASS side in which more fraction of columnar grains was observed as compared to the WZ near 439 FSS side in W1 weldment. The phase map shows a high fraction of austenite (97%) and very less ferrite fraction (2%). These low fraction of ferrite grains were mainly observed inside the WZ as well as HAZ region (Fig. 6e). Grain size map of the 304L ASS BM shows presence of large fraction of annealing twins and equiaxed grains. GS_{avg} was calculated for the 304L austenitic side region which shows the value of $\sim 116 \pm 100$ μm. GS_{avg} was nearly half for the austenitic side regions as compared to the ferritic side regions. Differences in the GS_{avg} could be due to the differences in thermal conductivity as well as initial grain
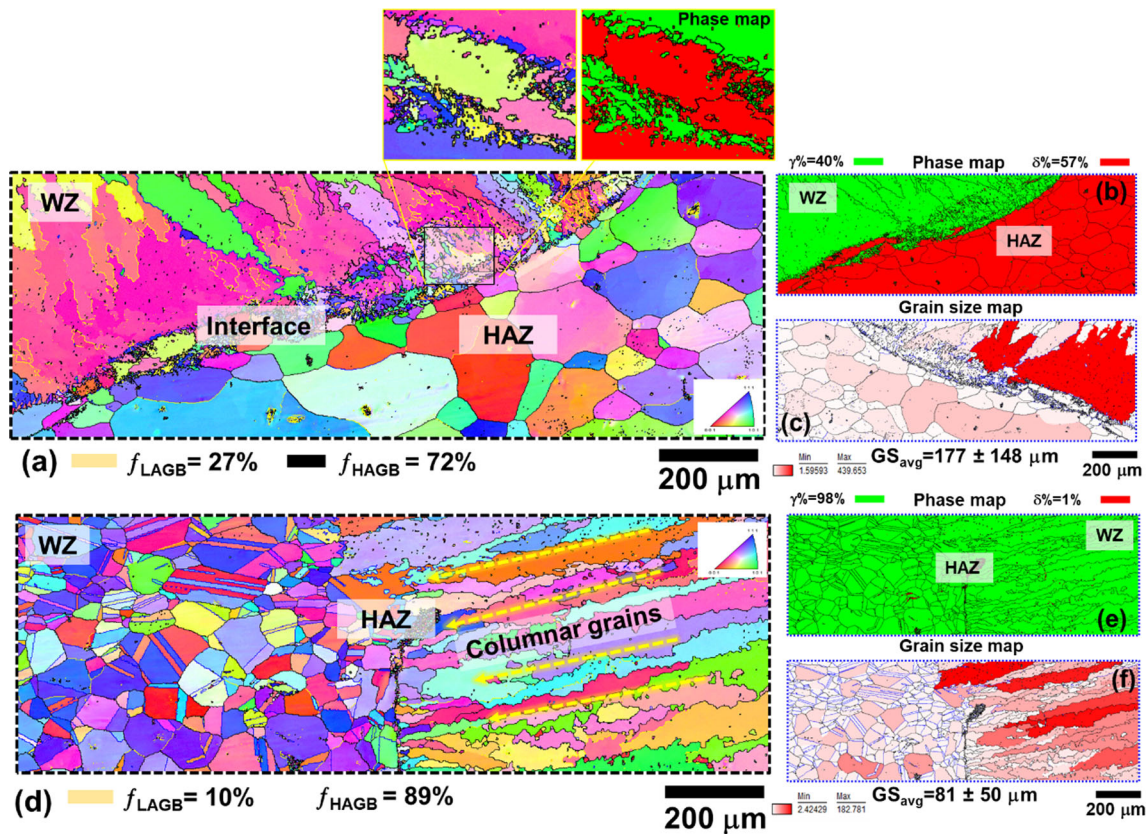
Fig. 7 (a-c) Inverse pole figure (IPF) map, phase map and grain size map of W2 weldment consisting the region of HAZ, WZ and interface between the HAZ and WZ. (d-f) IPF map, phase map and grain size map of W2 weldment consisting the region of WZ, 304L ASS BM and interface between the WZ and 304L ASS BM. *Note:* In phase map—red and green colour represent ferrite and austenite phase, respectively. Twin boundaries are the combined $\Sigma3 + \Sigma9$ boundaries (blue colour). Magnified region in (a) represent the IPF and phase maps at the interface between the HAZ and WZ (Color figure online)

sizes of 439 FSS BM and 304L ASS BM. Figure 7 shows the IPF, phase and grain size maps of the W2 weldment. Figure 7(a), (b) and (c) shows the evolved microstructure at the ferritic side of the W2 weldment. IPF map indicates the evolution of coarse grain for the FSS HAZ (i.e., CGHAZ region) and the columnar grains in the WZ. Columnar grains result of the direction solidification of the austenitic dendrites during the welding solidification. High magnification images in Fig. 7(a) refer to the interface region between CGHAZ and WZ. The evolution of very small size austenite grains (green colour grains) was observed around the coarse ferrite grains (red colour grains). Since, this region is WZ and hence, temperature variation could cause the nucleation of small sized austenites at the ferrite GBs (Fig. 7a). A similar fraction of austenite (~40%) and ferrite (~57%) phases was obtained in W2 as was observed for the W1 condition (Fig. 7b). Grain size map shows the variation in the GS of the columnar dendrites in the WZ in which coarse and fine grains are represented by dark red and light red colour, respectively (Fig. 7c).

GS$_{avg}$ for the regions near 439 FSS side is 177 ± 148 μm. No substantial difference was observed in the ferritic side of the microstructure between W1 and W2 weldments. Large and coarse dendritic grains could be because of a slow cooling rate which causes the grain growth to occur (Ref 32). Microstructure evolution near the 304L ASS side of the W2 weldment is shown in Fig. 7(d), (e) and (f). IPF map shows the columnar grains in the WZ and HAZ region which is not very much

separated from the 304L ASS BM. As discussed in Fig. 5(b) that interface between the WZ and HAZ (304L side) were showing the UMZ. However, these features of UMZ were not clearly observed in the IPF map. Grains evolved at the HAZ and 304L ASS BM seems to be similar as can be observed in the phase map (Fig. 7e). There was no indication of the ferrite phase in the HAZ region. Only 1% fraction was observed for the ferrite phase in the austenitic side of the W2 weldment (Fig. 7e). Grain size map infers the columnar nature of the austenite grains near the ASS side and GS$_{avg}$ was 81 ± 50 μm (Fig. 7f). Even, there was the variation in the HIs, but no variation was observed in the phase fraction in the phase maps between W1 and W2 weldments (Fig. 7d).

Variation in the GBs fraction as well as GS$_{avg}$ was observed between the W1 and W2 conditions. The ferritic region of W1 weldment shows 21% and 79% of LAGBs (3-15°) and HAGBs (>15°), respectively, whereas the similar region in W2 weldment showed 27% and 72% LAGBs and HAGBs fraction. Variation in the GBs fraction was due to changes in the HIs and thermal cycle for both the weldment conditions. Also, a difference was observed in the GS$_{avg}$ between both the weldments, which was due to different thermal cycles. Faster cooling in the W2 condition was attributed to smaller GS$_{avg}$ as compared to the W1 condition. Calculated GS$_{avg}$ for W2 weldments is nearly half of the values observed for W1 weldment. Figures 6 and 7 are giving the information about the evolved microstructure from the combined regions such as
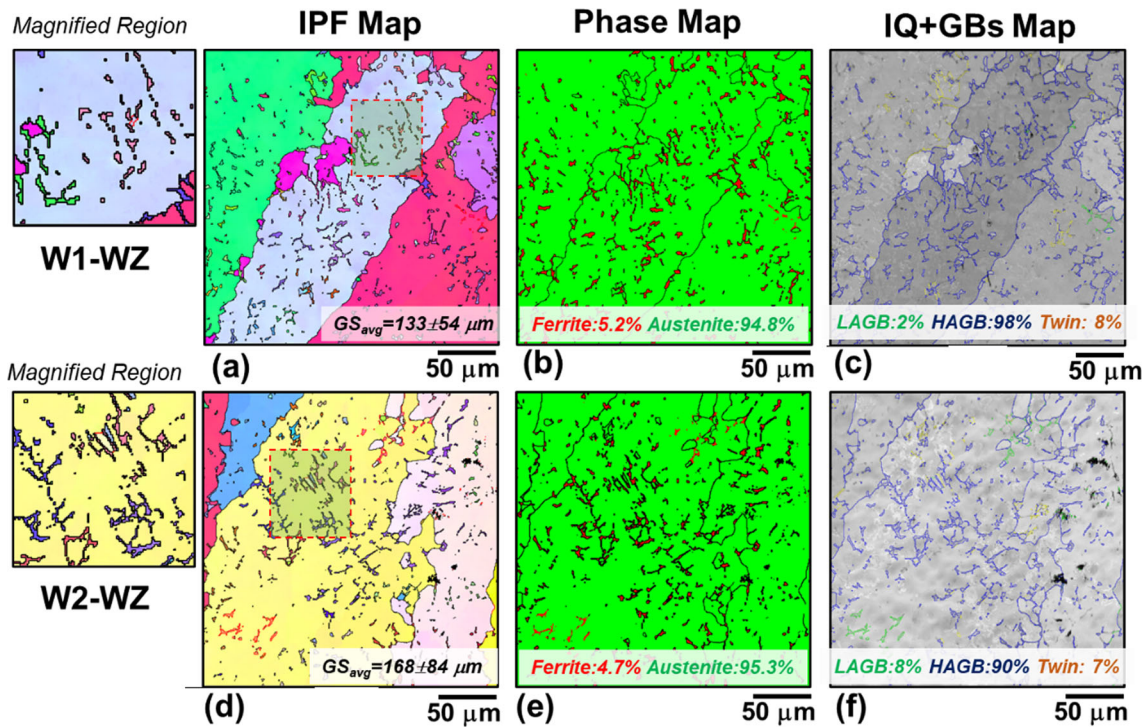
Fig. 8 (a-c) Inverse pole figure (IPF) map, phase map, and image quality (IQ) + GBs map of WZ region of W1 weldment. (d-f) Inverse pole figure (IPF) map, phase map, and image quality (IQ) + GBs map of WZ region of W2 weldment. *Note:* In phase map—red and green colour represent ferrite and austenite phase, respectively. Twin boundaries are the combined $\Sigma 3 + \Sigma 9$ boundaries (yellow colour) (Color figure online)

HAZ (439 FSS side) + WZ (Fig. 6a, b and c) or WZ + HAZ + 304L ASS (Fig. 6d, e and f). Hence, area specific measurements were also performed in which only WZ regions were considered for both the weldments.

Figure 8 illustrates the EBSD analysis (IPF, phase and IQ + GBs maps) of the WZ of the two different HIs. The presence of SF and LF in the austenite matrix in the W1-WZ and W2-WZ weldments can be observed in Fig. 8(a) and (d). Ferrite grains in W1-WZ and W2-WZ weldments shows the GS_{avg} value of $\sim$ 3-4 μm. The magnified microstructure of W1-WZ (Fig. 8a) shows very fine LF morphology as was discussed in (Fig. 3c). GS_{avg} for the W1-WZ was 133 $\pm$ 54 μm which was different from the GS_{avg} observed in Fig. 6(c) (286 $\pm$ 223 μm). Variation in the GS_{avg} would be due to consideration of the limited scan area for the high magnification image of Fig. 8. Notably, the GS_{avg} is the combined GS of the large austenite grains and small ferrite grains. Phase fraction of the W1-WZ and W2-WZ weldments was also calculated. Notably, not much variation is observed in the phase fractions in both the weldments; $\sim$ 95% austenite and $\sim$ 5% ferrite were observed in W1 and W2 conditions as shown in Fig. 8(b) and (e). However, a significant difference is noted in the phase fractions when calculated from EBSD and XRD techniques for both the weldments. From XRD analysis, the W1-WZ has 63% austenite, whereas W2-WZ has $\sim$ 67% austenite. XRD measurement is performed for the entire surface ($\sim 10 \times 10$ mm^2) with the sub-surface information, whereas EBSD measurement is the observation of features at the surface level. Further, from the phase map, it could be observed that the most of ferrite grains were nucleated inside the austenite grains, and very few ferrite grains were nucleated at the austenitic GBs (Fig. 8b and e)).

As the peppery structure was observed only in the FSS side of both weldments, SEM-EDS analysis (Fig. 9a and b) was performed to quantify the chemical compositions of the peppery features. It can be observed from the OM (Fig. 5c, d, e and f) and SEM (Fig. 9a and b) that the "peppery structure" concentration was higher in the W2 weldment as compared to the W1 weldment. The higher concentration of the "peppery structure" observed in the W2-HAZ can be attributed to the two reasons: (i) higher dissolution of C in the ferrite matrix, which leads to a higher number of supersaturation sites, providing favourable conditions for the formation of precipitates (Ref 19) and (ii) as suggested by Sarkari et al. (Ref 33) that the GBs may play a role in facilitating higher short-range diffusion. This enhanced diffusion along the GBs can contribute to the increased precipitate formation observed in the W2-HAZ. In the present investigation, it was observed that (Fig. 5d) the W2-HAZ is wider as compared to the W1-HAZ which contains a higher number of grains and GBs leading to a higher concentration of precipitates. Figure 9(a) and (b) illustrates the SEM-EDS analysis of the W1-HAZ and W2-HAZ of the FSS side. The presence of varying Cr and C contents in the ferrite grains and GBs can be observed. Notably, the EDS analysis indicated that the content of Cr and C was higher within the ferrite grains compared to the GBs. Consequently, it can be inferred that the precipitates formed in the HAZ of both weldments predominantly consist of carbide precipitates rich in Cr. Figure 9(c) depicts the XRD spectrums of both the weldments which include (BM, HAZ, and WZ region) to quantify the carbide phase in the HAZ. Notably, in addition to the peaks corresponding to austenite and ferrite, the presence of a peak associated with Cr carbide is observed in both weldments. This confirms that the peppery features
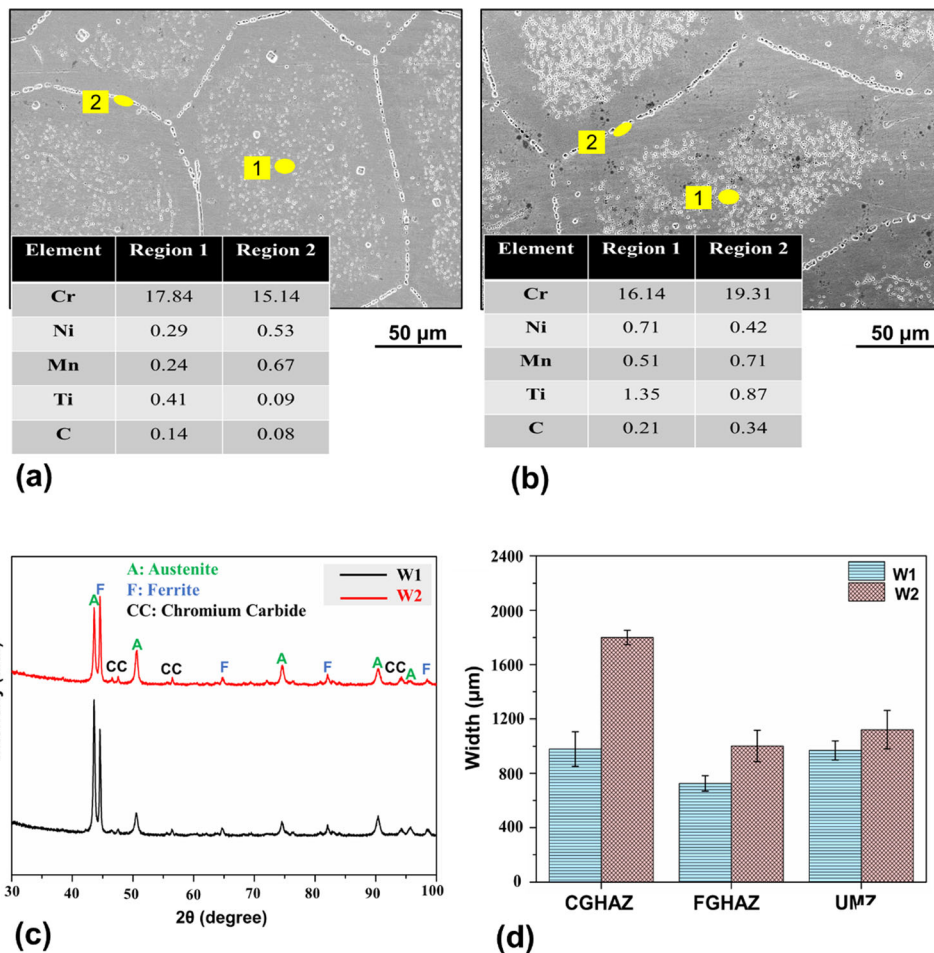
Fig. 9 SEM-EDS analysis of HAZ of (a) W1 and (b) W2 weldments (c) XRD spectrum of W1 and W2 weldments (d) Variation in the width of HAZ and UMZ of W1 and W2 weldments. *Note:* Region 1 represents the chemical compositions of chromium carbide precipitates and region 2 represents the chemical compositions of ferrite grain boundaries (GBs); W1-low HI, W2-high HI, and CC-chromium carbide (Color figure online)

observed in HAZ are indeed the result of the formation of a third phase. In previous results, it was observed that the peak of precipitates was absent in BMs (Fig. 2b and d) and WZ (Fig. 3e), which supports that the presence of an additional peak in Fig. 9(c) is the precipitate peaks of HAZ.

Figure 9(d) shows the graphical representations of the variation in the width of the HAZ (i.e., CGHAZ and FGHAZ) on the 439 FSS side as well as the width of the UMZ on the 304L ASS side. The width of the different regions was measured using the line intercept method using the multiple OMs. It can be seen that with an increase in HI, the width of the UMZ on the ASS side and the total width of the HAZ (CGHAZ and FGHAZ) on the FSS side were increased (Fig. 9d). Due to the slower cooling rate experienced by the W2 weldment, wider regions of HAZ on the FSS side and UMZ on the ASS side was observed. The results are consistent with the literatures (Ref 20, Ref 30).

3.2 Mechanical Properties

Figure 10(a) presents the difference in micro-hardness across various regions in both weldments. The discrepancies in micro-hardness values can be ascribed to the existence of various phases and precipitates with distinct volumetric proportions in different zones of the weldments. The average

micro-hardness values of the W1-WZ (334.32 HV) were observed to be 7.51% higher than that of the W2-WZ (310.92 HV) (Fig. 10a). This variation in micro-hardness values can be ascribed to the higher volumetric ferrite fraction in the W1-WZ than W2-WZ. Ferrite generally possesses greater hardness than austenite, and therefore, a higher fraction of ferrite with smaller GS_{avg} (as seen in Fig. 8a) resulted in increased micro-hardness (Ref 20, 34). When moving from WZ to the ASS side for both weldments, in UMZ, a slight increase in micro-hardness values was observed as compared to the WZ. However, no substantial variation in micro-hardness values was observed in the UMZ of both weldments. The increased micro-hardness values of the UMZ compared to the WZ are due to the formation of finer δ-ferrite stringers in the UMZ region, as depicted in Fig. 5(a) and (b) (Ref 35). Further, decreased micro-hardness was observed in ASS BM + HAZ for both weldments because of the absence of any precipitates and coarse grain size (Fig. 5a and b). The HAZ on the FSS side of both weldments exhibited differences in micro-hardness due to variations in the concentration of Cr-carbide. It was noticed that the average micro-hardness of the W2-HAZ (222.47 HV) was 6.71% higher than that in the W1-HAZ (208.52 HV), which can be attributed to the presence of higher amounts of Cr-carbide precipitates. Additionally, it was observed that FGHAZ (W1-218.9 HV, W2-231.93 HV) had a
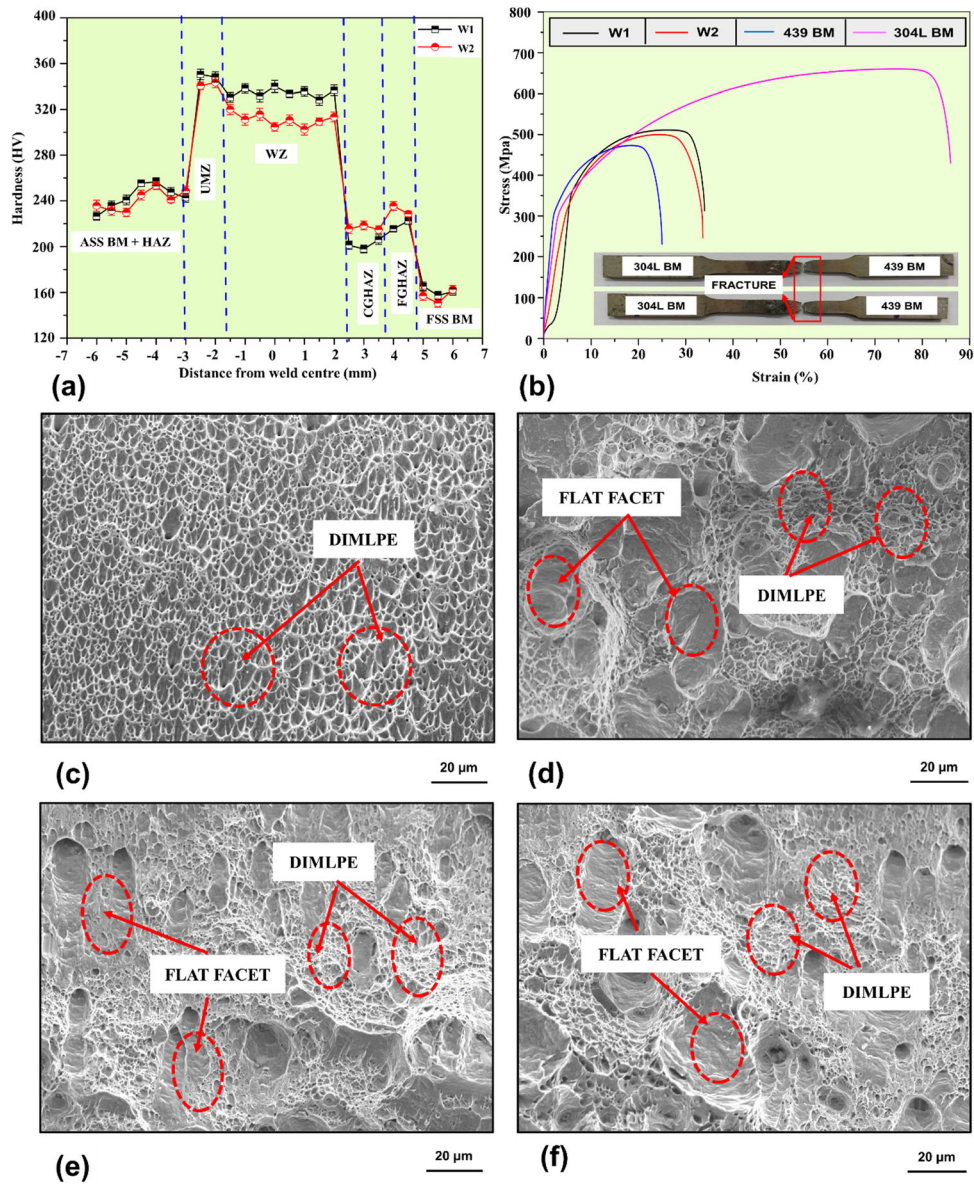
Fig. 10 (a) Microhardness profile of W1 (low HI) and W2 (high HI) weldments; (b) Stress-strain curve of BMs and weldments; SEM micrographs of fractures region (fractography) of (c) 304L BM, (d) 439 BM, (e) W1 weldment, and (f) W2 weldment (Color figure online)

higher average micro-hardness than CGHAZ (W1-201.6 HV, W2-216.61 HV), which was caused by the development of a finer grain microstructure in FGHAZ (Fig. 5c and d). The presence of carbide precipitates within the ferrite grains can make a substantial contribution to the observed increase in micro-hardness (Ref 19). Additionally, the WZ and HAZ regions for both weldments depicted enhanced micro-hardness than the 439 FSS BM.

Figure 10(b), (c), (d), (e) and (f) depicts the results of the tensile tests conducted on both the weldments and BMs, along with their respective stress-strain diagrams and fractography. The results of the tensile tests indicated that the W1 weldment exhibits higher ultimate tensile strength (UTS) and yield strength (YS) (UTS -511.23 ± 2.54 MPa, YS -347.45 ± 5.61 MPa) than W2 weldment (UTS -500.35 ± 3.54 MPa, YS -312.49 ± 4.51 MPa). According to reports, an increase in the ferrite fraction with finer grain structure was responsible for the improved tensile properties (Ref 23, 34). Ferrite is generally a

harder phase than austenite, which means that a higher critical resolved shear stress value is required to overcome the barriers presented by ferrite GBs than the austenite phase (Ref 36). This could be one of the causes of higher tensile strength of W1 since the weldment has a higher ferrite fraction than W2. Moreover, it is never preferred to have a WZ failure in a sound weld joint under a specified load condition because it could result in catastrophic failure. In the present study, as depicted in Fig. 10(b), for both weldments, the fracture occurred in 439 BM. Hence, it was concluded that both the weldments and 304L BM showed superior mechanical characteristics than 439 BM. The SEM analysis of the fractured surfaces of the tensile-tested specimens is presented in Fig. 10(c), (d), (e) and (f). In the fractography of the 304L BM, only dimples are observed. However, in the fractography of the 439 BM and both weldments, flat facets are also present in addition to dimples. The presence of flat facets and dimples on the fractography was directly related to the specimen's elongation (Ref 37). It was
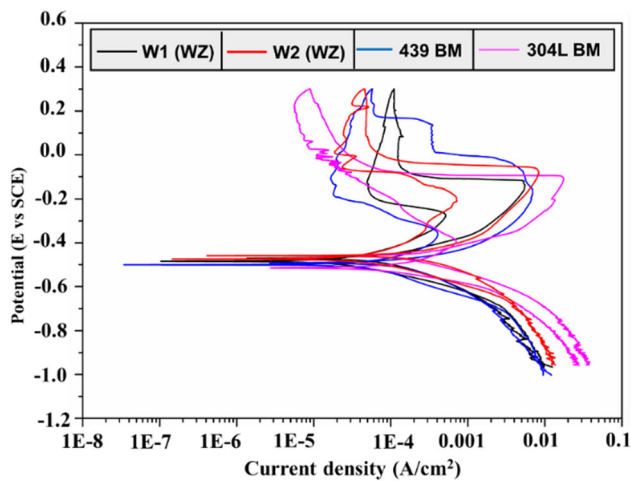
Fig. 11 DLEPR curves of BMs and WZ of W1 and W2 weldments (Color figure online)

Table 3 The DOS results obtained from the DLEPR test

Sample	I_a, 10^{-3}, A/cm^2	I_r, 10^{-3}, A/cm^2	DOS $(I_r/I_a)*100$
439 BM	6.9	0.40	5.79
304L BM	17.3	0.68	3.93
W1 (WZ)	5.3	0.49	9.24
W2 (WZ)	8.1	0.63	7.77

observed from Fig. 10(b) that the elongation was maximum (85 $\pm$ 2.54%) for 304L BM which decreased for W1 (33.80 $\pm$ 1.24%), W2 (33.58 $\pm$ 2.14%) and 439 BM (24.97 $\pm$ 1.38%). In this study, the 304L BM only depicted a dimple structure in its fractography (Fig. 10c), thus showing a ductile mode of failure. Further, 439 BM and both the weldments (Fig. 10d, e and f) depicted flat facets along with dimple structure, thus showing mixed mode (i.e. ductile as well as brittle mode) of fracture.

3.3 Corrosion Behaviour

3.3.1 Double-Loop Electrochemical Potentiodynamic Reactivation (DLEPR) Test Analysis. The susceptibility of welded samples and BMs toward IGC was examined using the DLEPR test. During the welding of SSs, the Cr-rich carbides or any other precipitate formation causes the depletion of Cr near the GBs (Ref 22). Hence, the GB attack is accelerated by Cr-depletion because it results in a potential difference between the grains and GBs. In the DLEPR test, the two scans, i.e. forward and reverse were performed. During a forward scan, H_2SO_4 passivates both the grains and GBs. The highest current achieved during this scan is referred to as the "activation current density (I_a)." During the reverse scan, the process of depassivation initiates, leading to the breakdown of the passive layer at the anodic sites or chromium-depleted areas. The passive film dissolves readily in these regions as the potential decreases. The maximum current observed during this scan is called the "reactivation current density (I_r)." The ratio of I_r/I_a is utilized to calculate the degree of sensitization (DOS) (Ref 20). Figure 11 displays the DLEPR curves for both the BMs and weldments, and the DPEPR test results are presented in Table 3. The presence of a single ferritic phase in 439 BM (Fig. 2(a), (b)) results in a higher DOS than 304L BM which consists single austenitic phase (Fig. 2(c), (d)). Previously, it has been reported that the FSS BM has greater DOS than the ASS BM (Ref 13). Additionally, studies have indicated that the austenite phase exhibits a reduced susceptibility to sensitization compared to the ferrite and martensite phases. This is attributed to the closely packed (FCC) structure of austenite, which results in higher activation energy compared to the loosely packed (BCC) structure of ferrite (Ref 38).

Furthermore, the DLEPR results for both weldments revealed that the DOS is higher in W1-WZ (9.24%) compared

to W2-WZ (7.77%), this difference is attributed to the higher ferrite fraction present in W1-WZ. In a dual-phase microstructure consisting of both austenite and ferrite phases, the ferrite phase is enriched with chromium, making it more susceptible to IGC (Ref 23). Moreover, Moon et al. (Ref 39) reported the formation of galvanic cells between the Cr-rich ferrite phase and the Cr-depleted austenite phase, which can contribute to IGC in corrosive environments. Therefore, it was concluded that the increased DOS in the WZ of W1 weldment is a result of the presence of a higher ferrite fraction.

3.3.2 Electrochemical Impedance Spectroscopy (EIS) Test Analysis. The resistance of the passive film in both BMs and WZ of the weldments was assessed by conducting the EIS test. Figure 12 depicts the EIS Nyquist and bode plots of all the specimens. The Nyquist experimental data were analysed by fitting the plots to the Randles equivalent circuit [R_s (CPE $\parallel$ R_{ct})], where R_s—solution resistance, CPE—constant phase element and R_{ct}—charge transfer resistance, as shown in Fig. 12(a). Figure 12(b) displays Nyquist plots, where the measured curve is represented by solid lines, and the calculated (fitted) curve is represented by symbols. The incomplete semicircles observed in the Nyquist plots (Fig. 12b) can be attributed to the charge transfer process taking place at the interface between the electrode and the electrolyte. This phenomenon is associated with changes in the properties of the film and an increase in the radius of impedance, indicates an enhancement in corrosion resistance (Ref 40). Further, a reduction in the radius of incomplete semicircles can be observed, indicating varying levels of corrosion resistance (Ref 41). Moreover, the values of R_{ct} offer an understanding of the electrochemical reaction rate happening at the interface between the protective film and the solution and a higher R_{ct} value indicates improved corrosion resistance (Ref 42). In a comparison of both the BMs, it was found that the R_{ct} values were higher for the 439 BM (R_{ct} −9385 $\pm$ 325.24 Ω cm^2) than the 304L BM (R_{ct} −8126 $\pm$ 235.87 Ω cm^2). Furthermore, it was noted that the impedance radius was greater for the W1-WZ, which showed a higher charge transfer resistance (R_{ct} −13545 $\pm$ 598.21 Ω cm^2) than the W2-WZ (R_{ct} −10688 $\pm$ 621.57 Ω cm^2). Also, the WZ of W1 weldment has higher Cr content resulting in the formation of more protective film, which increased the corrosion resistance. Consequently, the WZ of both weldments exhibited superior corrosion resistance in comparison to the BMs. In order to facilitate a more comprehensive interpretation of the EIS findings, bode and phase angle graphs (Fig. 12c) were obtained for the low and high frequency region.

In the bode plot, the impedance values in the range of lower frequency are indicative of corrosion resistance, whereas the impedance values in the range of higher frequency reflect the compactness or integrity of the passive film (Ref 43). The impedance value for the W1-WZ was found to be higher in
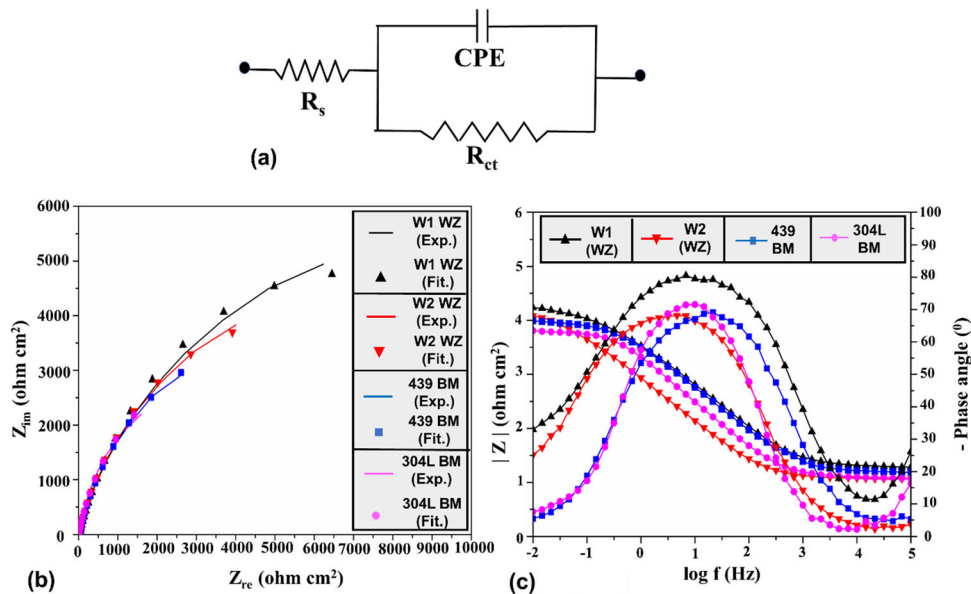
Fig. 12 (a) Electrical equivalent circuit for Nyquist curves of specimens, (b) Nyquist curves of BMs and WZ of W1 and W2 weldments, (b) Bode and phase angle curves of BMs and WZ of W1 and W2 weldments. *Note:* In Nyquist curves, solid lines represent experimental data and symbols represent fitted data (Color figure online)

both the lower and higher frequency regions, indicating higher corrosion resistance. Moreover, a decrease in impedance values was observed for W2-WZ, 439 BM, and 304L ASS, suggesting a decline in corrosion resistance. Additionally, the phase angle plot demonstrates variations in the phase angle as a function of frequency. When the phase angle values are below 90°, it signifies the presence of capacitive loops in the samples, indicating the formation of passive films in all the samples (Ref 23). According to reports, an increased phase angle is a clear indication of stronger resistance to charge transfer, which correlates directly with corrosion resistance (Ref 44). The variation in phase angle (Fig. 12c) revealed that W1-WZ exhibited the highest phase angle, implying that it possessed greater corrosion resistance compared to the others.

3.3.3 Potentiodynamic Polarization (PDP) Test Analysis. To assess the pitting corrosion resistance of the BMs and WZ of both weldments, a PDP test was conducted. When metal or alloy surfaces are exposed to a corrosive environment, the passive layer initially formed on the surface can break down. This breakdown leads to localized pitting at specific locations on the surface, where the dissolution of the material becomes accelerated (Ref 30). The pitting corrosion of metal and alloys can be analysed by PDP curves. These curves are plotted by measuring the potential and current density relationship, this plot is commonly referred to as a "Tafel plot." Figure 13(a) depicts the PDP curves of both the BMs as well as the WZ of W1 and W2 weldments. By applying the "Tafel fitting" method to the obtained curve, the corrosion potential (E_{corr}) and corrosion current density (i_{corr}) were determined. Figure 13(b) illustrates the changes in E_{corr} and i_{corr} values for both the BM and the WZ of both weldments. When comparing the BMs, it is evident that the 304L BM exhibits a higher i_{corr} (~ 1.85 μA/cm^2) compared to the 439 BM ($i_{corr} \sim 1.61$ μA/cm^2). Furthermore, the EIS Nyquist results (Fig. 12b) indicated that the 439 BM has a higher R_{ct} value than the 304L BM. Based on these

observations, it can be concluded that 439 BM demonstrates superior resistance to pitting corrosion compared to the 304L BM. According to previous reports, the austenite phase is considered the preferred site for pitting corrosion (Ref 23). Consequently, this leads to reduced corrosion resistance for the 304L BM than the 439 BM. Furthermore, the EIS results indicated that the W1-WZ exhibited a higher R_{ct} value, resulting in a lower i_{corr} value ($i_{corr} \sim 0.39$ μA/cm^2) as compared to the W2-WZ ($i_{corr} \sim 0.99$ μA/cm^2). The pitting resistance of the weldments can also be assessed using the pitting resistance equivalent number (PREN), as described in Eq 6 (Ref 30).

$$PREN = \% \, Cr + 16\% \, N + 3.3\% \, Mo \qquad (Eq \ 6)$$

In the current study, the pitting resistance of the BMs and filler electrode was primarily influenced by the Cr content since Mo and N were not present in these materials. In our present study, as stated previously, the W1-WZ weldment had higher ferrite fraction (36.86%) as compared to W2-WZ weldment (33.02%). As Cr is the ferrite stabilizer and the presence of higher ferrite fraction in W1-WZ may have resulted in the higher corrosion resistance as compared to W2-WZ. The presence of Cr aids in stabilizing the passive film, as mentioned in references (Ref 11, 21). Further, the corrosion resistance of the weldments was superior than the BMs.

Figure 13(c) and (d) depicts the pitting images obtained after the PDP test for the WZ of both weldments. The diameter of the pits was analysed through ImageJ software, and it was observed that the average diameter of pits of W1-WZ was (~ 109.96 μm) and the average diameter of pits of W2-WZ was (~ 186.68 μm). The reason for significant increased pit diameter of W2-WZ may be due to the formation of less protective passive film.
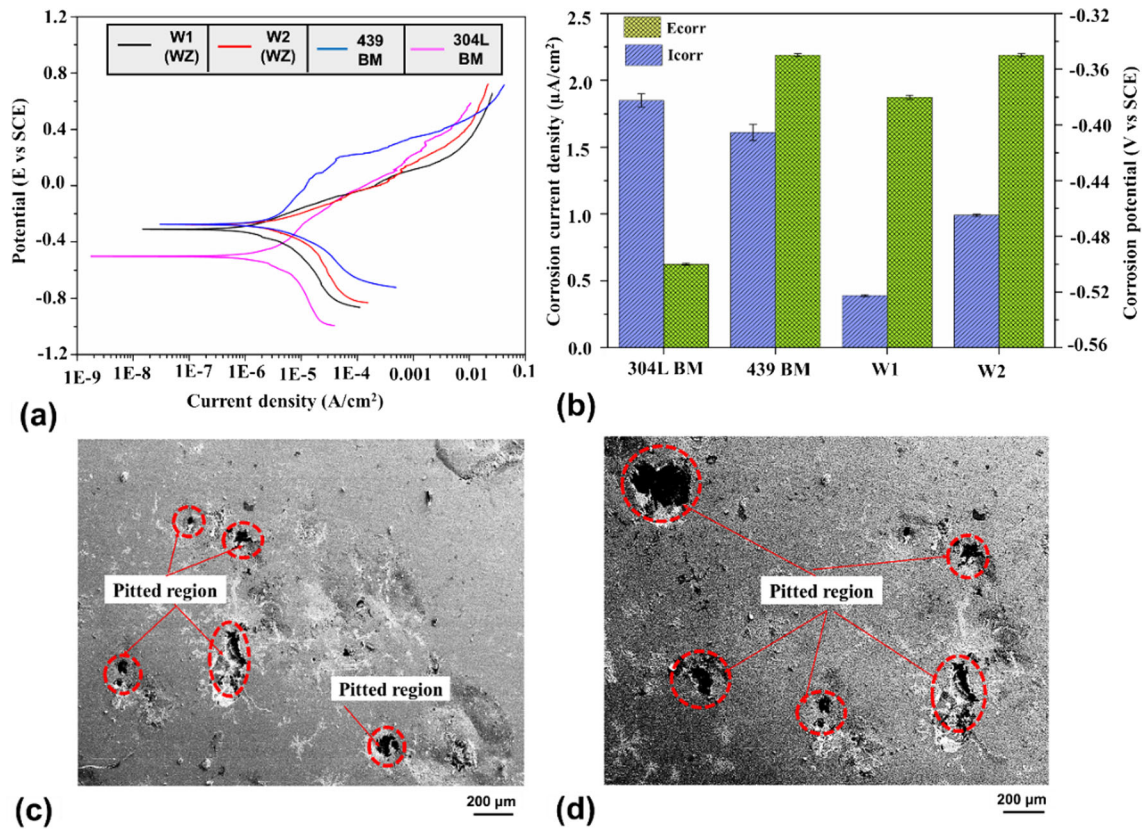
Fig. 13 (a) PDP curve of BMs, WZ of W1 and W2 weldments, (b) variation of I_{corr} and E_{corr} of BMs, WZ of W1 and W2 weldments; (c, d) pitting images of WZ of W1 and W2 weldments (Color figure online)

4. Conclusions

In this study, the CMT welding technique was utilized to weld the 304L ASS- 439 FSS by employing 309L as a filler electrode. Microstructural, mechanical, and electrochemical properties of the weldments were discussed based on the differences in the HIs. Moreover, EBSD technique was performed to analyse the detailed microstructural features, i.e. phase fraction, GBs fraction, GS calculation. Based on the findings, the following conclusions can be inferred:

1. The sound joints were prepared by varying HIs i.e. W1 (low HI) and W2 (high HI). As HI increased, the ferrite fraction in WZ decreased. The OM revealed the formation of LF in W1-WZ and SF in W2-WZ weldment. A decrease in the ferrite fraction from 36.86 → 33.02% was observed with an increase in HIs.
2. On the ASS side, UMZ was formed which contains δ-ferrite stringers and the HAZ is formed on the FSS side containing a peppery structure, which was quantified to be Cr-rich carbides. With an increase in HI, the width of both the UMZ and HAZ is tend to increase. GS_{avg} of the welded region was coarser for the W1 than W2 weldment. EBSD micrographs shows the coarse columnar austenite grains for the W1-WZ and W2-WZ weldments.
3. The W1 weldment exhibited a higher average micro-hardness (334.32 HV) in the WZ, whereas the W2 weldment had a lower average micro-hardness (310.92 HV) in the WZ. The enhanced mechanical properties of the W1 weldment can primarily be attributed to a higher fraction

of ferrite. In the case of the ASS BM, fracture occurred in a ductile manner. However, for both weldments and the FSS BM, a mixed mode of fracture, encompassing both ductile and brittle characteristics, was observed. The fractures in both weldments predominantly occurred within the region of the 439 FSS BM.
4. The results of the electrochemical tests demonstrated that the W1-WZ exhibited lower resistance to IGC (DOS-9.24%) than the W2-WZ (DOS-7.77%), which was attributed to a higher ferrite fraction. Conversely, a reverse trend was observed for impedance and pitting resistance, which were attributed to a higher PREN value.

Author Contributions

S.K.G. helped in methodology, investigation, and writing—original draft. A.P.P. contributed to conceptualization, project administration, writing—review and editing, and supervision. R.C.R. done project administration. V.T. done methodology,

Conflict of interest

The authors declare no competing interests.

Open Access

References

1. S. Saha, M. Mukherjee, and T.K. Pal, Microstructure, Texture, and Mechanical Property Analysis of Gas Metal Arc Welded AISI 304 Austenitic Stainless Steel, *J. Mater. Eng. Perform.*, 2015, **24**, p 1125–1139. https://doi.org/10.1007/s11665-014-1374-0

2. G.M. Reddy, T. Mohandas, A.S. Rao, and Y.V. Satyanarayana, Influence of Welding Processes on Microstructure and Mechanical Properties of Dissimilar Austenitic-Ferritic Stainless Steel Welds, *Mater. Manuf. Process.*, 2005, **20**(2), p 147–173. https://doi.org/10.1081/AMP-200041844

3. T. Oshima, Y. Habara, and K. Kuroda, Efforts to Save Nickel in Austenitic Stainless Steels, *ISIJ Int.*, 2007, **47**(3), p 359–364. https://doi.org/10.2355/isijinternational.47.359

4. M.O.H. Amuda, and S. Mridha, Grain Refinement and Hardness Distribution in Cryogenically Cooled Ferritic Stainless Steel Welds, *Mater. Des.*, 2013, **47**, p 365–371. https://doi.org/10.1016/j.matdes.2012.12.008

5. M. Arivarasu, D. Ramkumar Kasinath, and A. Natarajan, Effect of Continuous and Pulsed Current on the Metallurgical and Mechanical Properties of Gas Tungsten Arc Welded AISI 4340 Aeronautical and AISI 304 L Austenitic Stainless Steel Dissimilar Joints, *Mater. Res.*, 2015, **18**(1), p 59–77. https://doi.org/10.1590/1516-1439.269714

6. J. Verma, R.V. Taiwade, R. Kataria, and A. Kumar, Welding and Electrochemical Behavior of Ferritic AISI 430 and Austeno-Ferritic UNS 32205 Dissimilar Welds, *J. Manuf. Process.*, 2018, **34**(6), p 292–302. https://doi.org/10.1016/j.jmapro.2018.06.019

7. S. Emami, S. Sadeghi-Kanani, T. Saeid, and F. Khan, Dissimilar Friction Stir Welding of AISI 430 Ferritic and AISI 304L Austenitic Stainless Steels, *Civil Mech. Eng.*, 2020, **20**, p 1–16. https://doi.org/10.1007/s43452-020-00138-7

8. M. Rezaee Hajideh, M. Farahani, S.A.D. Alavi, and N. Molla Ramezani, Investigation on the Effects of Tool Geometry on the Microstructure and the Mechanical Properties of Dissimilar Friction Stir Welded Polyethylene and Polypropylene Sheets, *J. Manuf. Process.*, 2017, **26**, p 269–279. https://doi.org/10.1016/j.jmapro.2017.02.018

9. G.D.Q. Caetano, C.C. Silva, and M.F. Motta et al., Influence of Rotation Speed and Axial Force on the Friction Stir Welding of AISI 410S Ferritic Stainless Steel, *J. Mater. Process. Technol.*, 2018, **262**(2), p 430–436. https://doi.org/10.1016/j.jmatprotec.2018.07.018

10. A.K. Lakshminarayanan and V. Balasubramanian, Use of DL-EPR Test to Assess Sensitization Resistance of AISI 409M Grade Ferritic Stainless Steel Joints, *J. Mater. Eng. Perform.*, 2013, **22**(8), p 2293–2303. https://doi.org/10.1007/s11665-013-0521-3

11. S.K. Gupta, A.P. Patil, R.C. Rathod, V. Tandon, and A. Gupta, Characterization of Microstructure, Mechanical and Corrosion Response in AISI 304L and Ti-Stabilized 439 Stainless Steels Weld Joints, *J. Manuf. Process.*, 2023, **101**, p 721–736. https://doi.org/10.1016/j.jmapro.2023.05.107

12. S. Aguilar, R. Tabares, and C. Serna, Microstructural Transformations of Dissimilar Austenite-Ferrite Stainless Steels Welded Joints, *J Mater Phy Chem.*, 2013, **1**(4), p 65–68.

13. C. Tembhurkar, R. Kataria, S. Ambade, J. Verma, A. Sharma, and S. Sarkar, Effect of Fillers and Autogenous Welding on Dissimilar Welded 316L Austenitic and 430 Ferritic Stainless Steels, *J. Mater. Eng. Perform.*, 2021, **30**(2), p 1444–1453. https://doi.org/10.1007/s11665-020-05395-4

14. D. Arun and K.D. Ramkumar, Microstructural and Mechanical Characteristics of Cold Metal Transfer Weld Joints of UNS S32750, *J. Mater. Eng. Perform.*, 2021, **30**(11), p 8095–8107. https://doi.org/10.1007/s11665-021-06015-5

15. J.G. Roy, N. Yuvaraj, and Vipin, Effect of Welding Parameters on Mechanical Properties of Cold Metal Transfer Welded Thin AISI 304 Stainless-Steel Sheets, *Trans. Ind. Inst. Metals.*, 2021, **74**(9), p 2397–2408. https://doi.org/10.1007/s12666-021-02326-2

16. Y. Koli, N. Yuvaraj, Vipin, and S. Aravindan, Investigations on Weld Bead Geometry and Microstructure in CMT, MIG Pulse Synergic and MIG Welding of AA6061-T6, *Mater. Res. Exp.*, 2019, **6**(12), p 12655.

17. J. Frostevarg, A.F.H. Kaplan, and J. Lamas, Comparison of CMT with Other Arc Modes for Laser-Arc Hybrid Welding of Steel, *Weld World.*, 2014, **58**(5), p 649–660. https://doi.org/10.1007/s40194-014-0146-7

18. B.Y. Dharmik and N.K. Lautre, Performance Assessment of CMT Over GTA Welding on Stacked Thin Sheets of CRNGO Electrical Steel, *Mater. Lett.*, 2020, **272**, 127901. https://doi.org/10.1016/j.matlet.2020.127901

19. J. Zhou, J. Shen, S. Hu, G. Zhao, and Q. Wang, Microstructure and Mechanical Properties of AISI 430 Ferritic Stainless Steel Joints Fabricated by Cold Metal Transfer Welding, *Mater. Res. Exp.*, 2019 https://doi.org/10.1088/2053-1591/ab4770

20. S.K. Gupta, A.P. Patil, R.C. Rathod, V. Tandon, and H. Vashishtha, Tailoring the Process Parameters for Ti-Stabilized 439 Ferritic Stainless Steel Welds by Cold Metal Transfer Process, *J. Mater. Eng. Perform.*, 2023, **32**, p 6042–6053. https://doi.org/10.1007/s11665-022-07534-5

21. N. Jahanzeb, J.H. Shin, J. Singh, Y.U. Heo, and S.H. Choi, Effect of Microstructure on the Hardness Heterogeneity of Dissimilar Metal Joints Between 316L Stainless Steel and SS400 Steel, *Mater. Sci. Eng. A*, 2017, **700**, p 338–350.

22. S.K. Gupta, A.P. Patil, R.C. Rathod, V. Tandon, and H. Vashishtha, Investigation on Impact of Heat Input on Microstructural, Mechanical, and Intergranular Corrosion Properties of Gas Tungsten Arc-Welded Ti-Stabilized 439 Ferritic Stainless Steel, *J. Mater. Eng. Perform.*, 2022, **31**, p 4084–4097. https://doi.org/10.1007/s11665-021-06512-7

23. A.V. Bansod, A.P. Patil, A.P. Moon, and S. Shukla, Microstructural and Electrochemical Evaluation of Fusion Welded Low-Nickel and 304 SS at Different Heat Input, *J. Mater. Eng. Perform.*, 2017, **26**(12), p 5847–5863. https://doi.org/10.1007/s11665-017-3054-3

24. A. Eghlimi, M. Shamanian, M. Eskandarian, A. Zabolian, M. Nezakat, and J.A. Szpunar, Evaluation of Microstructure and Texture Across the Welded Interface of Super Duplex Stainless Steel and High Strength Low Alloy Steel, *Surf. Coat. Technol.*, 2015, **264**, p 150–162. https://doi.org/10.1016/j.surfcoat.2014.12.060

25. S.K. Gupta, A.R. Raja, M. Vashista, and M.Z.K. Yusufzai, Effect of Heat Input on Microstructure and Mechanical Properties in Gas Metal Arc Welding of Ferritic Stainless Steel Mater, *Res. Exp.*, 2019 https://doi.org/10.1088/2053-1591/aaf492

26. J.C. Lippold and D.J. Kotecki, *Welding Metallurgy and Weldability of Stainless Steel*, John Wiley and Sons, Hoboken, 2005

27. S. Sabooni, F. Karimzadeh, M.H. Enayati, A.H.W. Ngan, and H. Jabbari, Gas Tungsten Arc Welding and Friction Stir Welding of Ultrafine Grained AISI 304L Stainless Steel: Microstructural and

Mechanical Behavior Characterization, *Mater. Char.*, 2015, **109**, p 138–151. https://doi.org/10.1016/j.matchar.2015.08.009

28. S.K. Gupta, A.P. Patil, R.C. Rathod, V. Tandon, A. Gupta, and J. Chavhan, Influence of Filler Variation on Microstructural Evolution, Mechanical and Corrosion Performance of Ti-Stabilized 439 Ferritic Stainless Steel, *Mater. Today Commun.*, 2022, **34**(8), 105010. https://doi.org/10.1016/j.mtcomm.2022.105010

29. H.S. Hosseini, M. Shamanian, and A. Kermanpur, Characterization of Microstructures and 3mechanical Properties of Inconel 617/310 Stainless Steel Dissimilar Welds, *Mater. Chara.*, 2011, **62**, p 425–431.

30. J. Verma and R.V. Taiwade, Effect of Austenitic and Austeno-Ferritic Electrodes on 2205 Duplex and 316L Austenitic Stainless Steel Dissimilar Welds, *J. Mater. Eng. Perform.*, 2016, **25**(11), p 4706–4717. https://doi.org/10.1007/s11665-016-2329-4

31. M. Alizadeh-Sh, S.P.H. Marashi, and M. Pouranvari, Resistance Spot Welding of AISI 430 Ferritic Stainless Steel: Phase Transformations and Mechanical Properties, *J. Mater. Des.*, 2014, **56**, p 258–263. https://doi.org/10.1016/j.matdes.2013.11.022

32. J. Li, H. Li, Y. Liang, P. Liu, and L. Yang, The Microstructure and Mechanical Properties of Multi-Strand, Composite Welding-Wire Welded Joints of High Nitrogen Austenitic Stainless Steel, *Materials.*, 2019, **12**, p 2944. https://doi.org/10.3390/ma12182944

33. M.S. Khorrami, M.A. Mostafaei, and H. Pouraliakbar, Study on Microstructure and Mechanical Characteristics of Low-Carbon Steel and Ferritic Stainless Steel Joints, *Mater. Sci. Eng. A*, 2014, **608**, p 35–45. https://doi.org/10.1016/j.msea.2014.04.065

34. W. Chuaiphan and L. Srijaroenpramong, Optimization of TIG Welding Parameter in Dissimilar Joints of Low Nickel Stainless Steel AISI 205 and AISI 216, *J. Manuf. Process.*, 2020, **58**, p 163–178. https://doi.org/10.1016/j.jmapro.2020.07.052

35. S. Kumar and A.S. Shahi, Effect of Heat Input on the Microstructure and Mechanical Properties of Gas Tungsten Arc Welded AISI 304 Stainless Steel Joints, *Mater. Des.*, 2011, **32**(6), p 3617–3623. https://doi.org/10.1016/j.matdes.2011.02.017

36. M. Mlikota and S. Schmauder, On the Critical Resolved Shear Stress and Its Importance in the Fatigue Performance of Steels and Other Metals with Different Crystallographic Structures, *Metals.*, 2018 https://doi.org/10.3390/met8110883

37. E. Amiri, F. Ostovan, M. Toozandehjani, and E. Shafiei, Study and Selection of Most Appropriate Filler Rod for GTAW of S32750 Super Duplex Steel Joints: A Comprehensive Study on Microstructural, Mechanical and Corrosion Properties, *Mater. Chem Phy.*, 2021, **270**, 124839

38. L. Guo, G. Hua, B., and Yang et al., Electron Work Functions of Ferrite and Austenite Phases in a Duplex Stainless Steel and their Adhesive Forces with AFM Silicon Probe, *Sci. Rep.*, 2016, **6**, p 1–7.

39. J. Moon, H.Y. Ha, and T.H. Lee, Corrosion Behaviour in High Heat Input Welded Heat-Affected Zone of Ni-Free High-Nitrogen Fe-18Cr-10Mn-N Austenitic Stainless Steel, *Mater. Charact.*, 2013, **82**, p 113–119. https://doi.org/10.1016/j.matchar.2013.05.011

40. H. Zhao, Z. Zhang, H. Zhang, J. Hu, and J. Li, Effect of Aging Time on Intergranular Corrosion Behaviour of a Newly Developed LDX 2404 Lean Duplex Stainless Steel, *J. Alloys Compd.*, 2016, **672**, p 147–154. https://doi.org/10.1016/j.jallcom.2016.02.101

41. V. Tandon and A.P. Patil, On the Influence of Cold Working and Electrochemical Nitridation on the Corrosion Behaviour of 316L Austenitic Stainless Steel in Acidic Environment, *Surf. Eng. App. Electro.*, 2020, **56**(1), p 63–70. https://doi.org/10.3103/S1068375520010147

42. V. Tandon, A.P. Patil, and R.C. Rathod, Correlation of Martensite Content and Dislocation Density of Cold Worked 316L on Defect Densities of Passivating Film in Acidic Environment, *Mater. Res. Exp.*, 2018 https://doi.org/10.1088/2053-1591/aacee9

43. V. Tandon, M.A. Thombre, A.P. Patil, R.V. Taiwade, and H. Vashishtha, Effect of Heat Input on the Microstructural, Mechanical, and Corrosion Properties of Dissimilar Weldment of Conventional Austenitic Stainless Steel and Low - Nickel Stainless Steel, *Metallo. Micro. Analysis.*, 2020 https://doi.org/10.1007/s13632-020-00681-y

44. Y. Huang, J. Huang, and J. Zhang et al., Microstructure and Corrosion Characterization of Weld Metal in Stainless Steel and Low Carbon Steel Joint Under Different Heat Input, *Mater. Today Commun.*, 2021 https://doi.org/10.1016/j.mtcomm.2021.102948